TOPOLOGICAL MATTER

Helical quantum Hall phase in graphene on $SrTiO_3$

Louis Veyrat[1], Corentin Déprez[1], Alexis Coissard[1], Xiaoxi Li[2,3,4], Frédéric Gay[1], Kenji Watanabe[5], Takashi Taniguchi[5], Zheng Han[2,3,4], Benjamin A. Piot[6], Hermann Sellier[1], Benjamin Sacépé[1]*

The ground state of charge-neutral graphene under perpendicular magnetic field was predicted to be a quantum Hall topological insulator with a ferromagnetic order and spin-filtered, helical edge channels. In most experiments, however, an insulating state is observed that is accounted for by lattice-scale interactions that promote a broken-symmetry state with gapped bulk and edge excitations. We tuned the ground state of the graphene zeroth Landau level to the topological phase through a suitable screening of the Coulomb interaction with the high dielectric constant of a strontium titanate ($SrTiO_3$) substrate. Robust helical edge transport emerged at magnetic fields as low as 1 tesla and withstanding temperatures up to 110 kelvin over micron-long distances. This versatile graphene platform may find applications in spintronics and topological quantum computation.

Topological phases are classified by their dimensionality, symmetries, and topological invariants (*1*, *2*). In materials that exhibit these phases, the topological bulk gap closes at every interface with vacuum or a trivial insulator, forming conductive edge states with peculiar transport and spin properties. For example, the quantum Hall effect, which arises in two-dimensional (2D) electron systems subjected to a perpendicular magnetic field, B, is characterized by a Chern number that quantizes the Hall conductivity and counts the number of chiral, 1D edge channels. The distinctive aspect of quantum Hall systems compared with time-reversal symmetric topological insulators (TIs) lies in the role of Coulomb interaction between electrons that can induce a wealth of strongly correlated, topologically or symmetry-protected phases, ubiquitously observed in various experimental systems (*3*–*12*).

In graphene, the immediate consequence of the Coulomb interaction is an instability toward quantum Hall ferromagnetism. Owing to exchange interaction, a spontaneous breaking of the SU(4) symmetry splinters the Landau levels into quartets of broken-symmetry states that are polarized in spin or valley degrees of freedom or a combination of the two (*13*–*15*).

Central to this phenomenon is the fate of the zeroth Landau level and its quantum Hall ground states. It was predicted early that if the Zeeman spin splitting (enhanced by exchange interaction) overcomes the valley splitting, a topological inversion between the lowest electron-type and highest hole-type sublevels should occur (*16*, *17*). At charge neutrality, the ensuing ground state is a quantum Hall ferromagnet with two filled states of identical spin polarization and an edge dispersion that exhibits two counter-propagating, spin-filtered helical edge channels (Fig. 1, A and B), similar to those of the quantum spin Hall (QSH) effect in 2D TIs (*18*–*22*). Such a spin-polarized ferromagnetic (F) phase belongs to the recently identified class of interaction-induced TIs with zero Chern number, termed quantum Hall topological insulators (QHTIs) (*23*), which arise from a many-body interacting Landau level and can be pictured as two independent copies of quantum Hall systems with opposite chiralities. Notably, unlike 2D TIs, immunity of the helical edge channels to quasiparticles backscattering does not rely on the discrete time-reversal symmetry, conspicuously broken here by the magnetic field, but on the continuous U(1) axial rotation symmetry of the spin polarization (*8*, *23*).

The experimental situation is, however, at odds with this exciting scenario: A strong insulating state is consistently observed on increasing perpendicular magnetic field in charge-neutral, high-mobility graphene devices (*5*, *6*, *8*, *15*). The formation of the F phase is presumably hindered by lattice-scale electron-electron and electron-phonon interaction

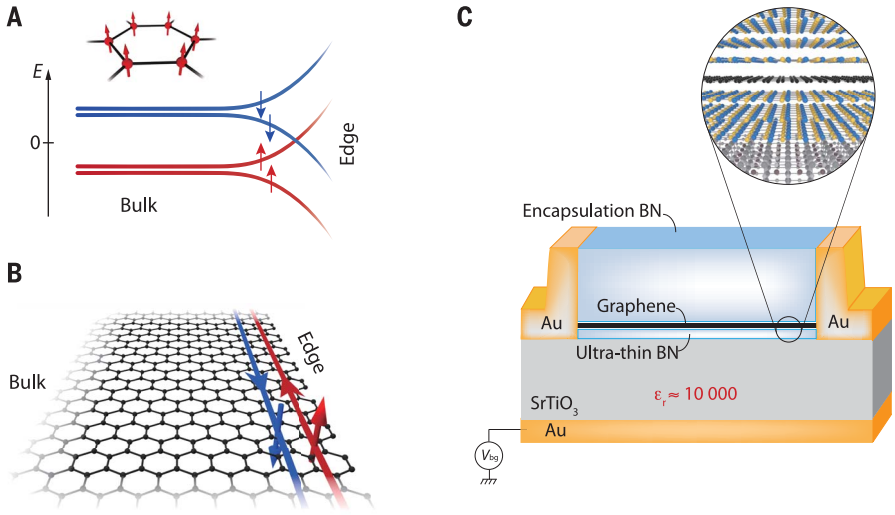

Fig. 1. Spin-polarized ferromagnetic phase in graphene on high-*k* dielectric. (**A**) In the ferromagnetic phase of charge-neutral graphene, the broken-symmetry state of the half-filled zeroth Landau level is spin polarized and occupies both sublattices of the honeycomb lattice, as shown in the inset. The edge dispersion results from linear combinations of the bulk isospin states, which disperse as electron-like and hole-like branches, yielding a pair of counter-propagative, spin-filtered helical edge channels at charge neutrality (*16*, *44*). Red and blue arrows represent the spin polarization of the sublevels. (**B**) Schematic of a graphene lattice with helical edge channels propagating on the crystallographic armchair edge. (**C**) Schematic of the hBN-encapsulated graphene device placed on a $SrTiO_3$ substrate that serves both as a high–dielectric constant environment and a back-gate dielectric. Owing to the considerable dielectric constant (ε_r ~ 10,000) of the $SrTiO_3$ substrate at low temperature and the ultrathin hBN spacer (2 to 5 nm thick), Coulomb interaction in the graphene plane is substantially screened, resulting in a modification of the quantum Hall ground state at charge neutrality and the emergence of the ferromagnetic phase with helical edge transport. The magnified view shows atomic layers of the hBN-encapsulated graphene van der Waals assembly and the surface atomic structure of $SrTiO_3$.

[1]Université Grenoble Alpes, CNRS, Grenoble INP, Institut Néel, 38000 Grenoble, France. [2]Shenyang National Laboratory for Materials Science, Institute of Metal Research, Chinese Academy of Sciences, Shenyang 110016, P. R. China. [3]School of Material Science and Engineering, University of Science and Technology of China, Anhui 230026, P. R. China. [4]State Key Laboratory of Quantum Optics and Quantum Optics Devices, Institute of Opto-Electronics, Shanxi University, Taiyuan 030006, P. R. China. [5]National Institute for Materials Science, 1-1 Namiki, Tsukuba 306-0044, Japan. [6]Université Grenoble Alpes, UPS-INSA-EMFL-CNRS-LNCMI, 38000 Grenoble, France.
*Corresponding author. Email: benjamin.sacepe@neel.cnrs.fr

terms, whose amplitudes and signs can be strongly renormalized by the long-range part of the Coulomb interaction (*24*), favoring various insulating spin- or charge-density-wave orders (*24*–*28*). Only with a very strong in-plane magnetic-field component higher than 30 T such that Zeeman energy overcomes the other anisotropic interaction terms does the F phase emerge experimentally (*7*, *8*). Another strategy to engineer an F phase uses misaligned graphene bilayers with the two layers hosting different quantum Hall states of opposite charge-carriers types (*29*). Yet, those approaches suffer from either an unpractically strong and tilted magnetic field or the complexity of the twisted layers assembly.

Here, we use a different approach to induce the F phase in monolayer graphene in a straightforward fashion. Instead of boosting the Zeeman effect with a strong in-plane field, we modify the effects of the lattice-scale interaction terms by a suitable substrate screening of the Coulomb interaction to restore the dominant role of the spin-polarizing terms and induce the F phase. We use a high–dielectric constant substrate, the quantum paraelectric $SrTiO_3$ known to exhibit a very large static dielectric constant of the order of $\epsilon \approx 10^4$ at low temperatures (*30*) (see fig. S3), which acts as both an electrostatic screening environment and a back-gate dielectric (*31*). For an efficient screening of the long-range Coulomb potential, the graphene layer must be sufficiently close to the substrate, with a separation less than the magnetic length $l_B = \sqrt{\hbar/eB}$ (where $\hbar$ is the reduced Planck constant and e is the electron charge), which is the relevant length scale in the quantum Hall regime. Such a screening indirectly affects the short-range, lattice-scale interaction terms through renormalization effects (*24*), eventually modifying the ground state of graphene at charge neutrality. To achieve this, we fabricated high-mobility graphene heterostructures based on hexagonal boron nitride (hBN) encapsulation (*32*), using an ultrathin bottom hBN layer. The bottom layer thickness d_{BN} ranged between 2 and 5 nm [see Fig. 1C and (*33*)], which is smaller than the magnetic length for moderate magnetic field (e.g., $l_B > 8$ nm for $B < 10$ T).

The emergence of the F phase in such a screened configuration is readily seen in Fig. 2A, which displays the two-terminal resistance R_{2t} of a hBN-encapsulated graphene device in a six-terminal Hall bar geometry, as a function of the back-gate voltage V_{bg} and magnetic field. Around the charge neutrality ($V_{bg} \sim 0$ V), an anomalous resistance plateau develops over a B range from 1.5 to 4 T, indicated by

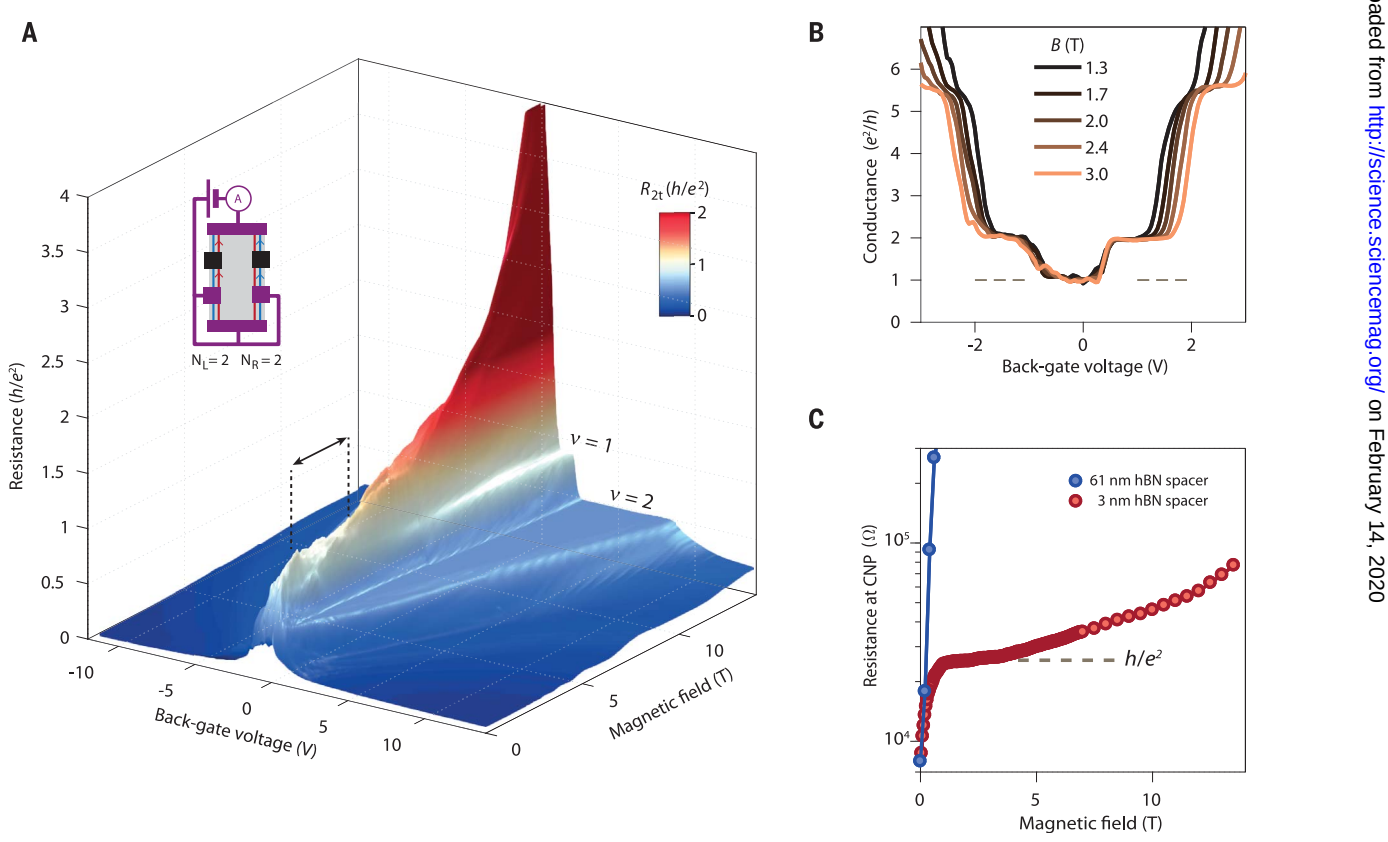

Fig. 2. Low–magnetic field quantum spin Hall effect. (**A**) Two-terminal resistance R_{2t} in units of h/e^2 of sample BNGrSTO-07 versus magnetic field and back-gate voltage measured at 4 K. In addition to standard quantum Hall plateaus at filling fractions ν = 1 and 2, the resistance exhibits an anomalous plateau around the charge neutrality point between B = 1.5 and 4 T, delimited by the black dashed lines and the double-headed arrow, which signals the regime of the QSH effect in this sample. The value of the resistance at this plateau is h/e^2 and is color coded white. The inset schematic indicates the contact configuration. Black contacts are floating. The red and blue arrows on the helical edge channels indicate the direction of the current between contacts, and A indicates the ampere meter. (**B**) Two-terminal conductance $G_{2t} = 1/R_{2t}$ in units of e^2/h versus back-gate voltage extracted from (A) at different magnetic fields. The first conductance plateaus of the quantum Hall effect at $2e^2/h$ and $6e^2/h$ are well defined. The QSH plateau of conductance e^2/h clearly emerges at charge neutrality around V_{bg} = 0 V. (**C**) Resistance at the charge neutrality point (CNP) versus magnetic field for sample BNGrSTO-07 (red dots) extracted from (A) and sample BNGrSTO-09 (blue dots). The latter sample has a thick hBN spacer and exhibits a strong positive magnetoresistance at low magnetic field diverging toward insulation; the sample with the thin hBN spacer (BNGrSTO-07) shows a QSH plateau that persists up to ~4 T, followed by a resistance increase at higher magnetic field. Ω, ohms.

the two dashed black lines. This plateau reaches the quantum of resistance h/e^2, color coded white, where h is the Planck constant. At $B > 5$ T, the resistance departs from h/e^2 toward insulation, as seen by the red color-coded magneto-resistance peak (see also Fig. 2C).

The unusual nature of this resistance plateau can be captured with the line cuts of the two-terminal conductance $G_{2t} = 1/R_{2t}$ versus V_{bg} at fixed B, (see Fig. 2B). In addition to the standard graphene quantum Hall plateaus at $G_{2t} = 4\frac{e^2}{h}\left(N + \frac{1}{2}\right) = 2e^2/h$ and $6e^2/h$ for the Landau level indices $N = 0$ and $N = 1$, which are well developed as a function of back-gate voltage (notice that the $N = 1$ plateau reaches 5.6 e^2/h instead of 6 e^2/h owing to the series resistances of the wiring in the experimental setup, which add up in the two-terminal configuration), the new plateau at $G_{2t} = e^2/h$ is centered at the charge neutrality and does not show any dip at $V_{bg} = 0$ V. This behavior is at odds with the usual sequence of broken-symmetry states setting with magnetic field where first the insulating broken-symmetry state opens at filling fraction $\nu = 0$ with $G_{2t} = 0$, followed at higher fields by the plateaus of the broken-symmetry states at $\nu = \pm 1$ (*14*, *15*). In Fig. 2A, the states at $\nu = \pm 1$ arise for $B > 6$ T together with the insulating magnetoresistance peak at $\nu = 0$, that is, above the field range of the anomalous plateau. Hence, this observation of a h/e^2 plateau at low magnetic field conspicuously points to a distinct broken-symmetry state at $\nu = 0$. We show below that this h/e^2 plateau is a direct signature of the QSH effect resulting from the helical edge channels of the F phase.

Helical edge transport has unambiguous signatures in multiterminal device configuration because each ohmic contact acts as a source of back-scattering for the counter-propagating helical edge channels with opposite spin polarization (*34*). An edge section between two contacts is indeed an ideal helical quantum conductor of quantized resistance h/e^2. The two-terminal resistance of a device therefore ensues from the parallel resistance of both edges, each of them being the sum of contributions of each helical edge section. As a result

$$R_{2t} = \frac{h}{e^2}\left(\frac{1}{N_L} + \frac{1}{N_R}\right)^{-1} \quad (1)$$

where N_L and N_R are, respectively, the number of helical conductor sections for the left (L) and right (R) edges between the source and drain contacts (*8*). By changing the source and drain contacts to correspond to various configurations of N_L and N_R, one expects to observe resistance plateaus given by Eq. 1. Figure 3A displays a set of four different configurations of two-terminal resistances measured at $B = 2.5$ T as a function of back-gate voltage. Changing the source and drain contacts and the number of helical edge sections (see contact configurations in Fig. 3B) yields a maximum around charge neutrality that reaches the expected values indicated by the dashed lines, thereby demonstrating helical edge transport. Notice that the plateau at h/e^2 in Fig. 2A is fully consistent with Eq. 1 for $N_L = N_R = 2$.

Four-terminal nonlocal configuration provides another stark indicator for helical edge transport (*34*). Figure 3C shows simultaneous measurements of the two-terminal resistance between the two blue contacts (see sample schematic in the inset) and the nonlocal resistance R_{NL} measured on the red contacts while keeping the same source and drain current-injection contacts. Whereas R_{2t} nearly reaches the expected value indicated by the dashed line, namely $\frac{5}{6}\frac{h}{e^2}$ ($N_L = 5$ and $N_R = 1$), a nonlocal voltage develops in the V_{bg} range that coincides with the helical edge transport regime in R_{2t}. The large value of this nonlocal signal, which

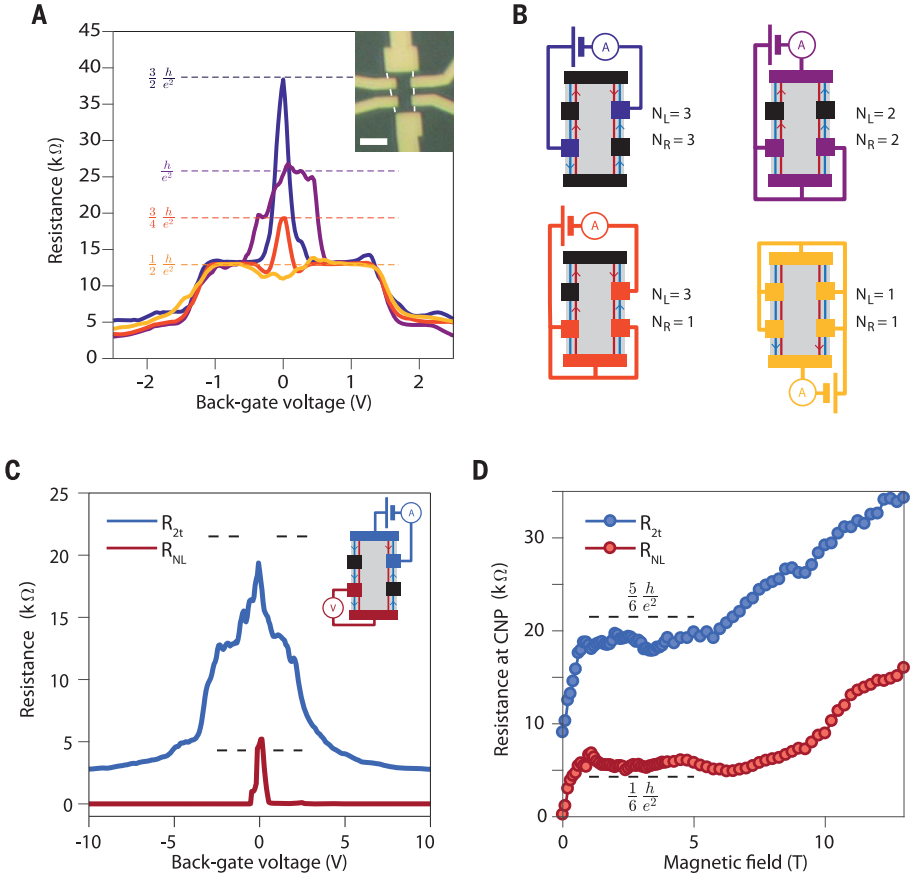

Fig. 3. Nonlocal helical edge transport. (**A**) Two-terminal resistance versus back-gate voltage measured at 2.5 T and 4 K for different contact configurations schematized in (B). The inset shows an optical picture of the measured sample BNGrSTO-07. The scale bar is 4 μm. Each contact configuration yields a resistance at charge neutrality reaching the expected values for helical edge transport, which are indicated with the horizontal dashed lines. (**B**) Schematics of the measurement configurations. Black contacts are floating. The red and blue arrows on the helical edge channels indicate the direction of the current between contacts. (**C**) Two-terminal resistance, R_{2t}, in blue and nonlocal, four-terminal resistance, R_{NL}, in red versus back-gate voltage in the contact configuration shown in the inset schematic. In the schematic, V indicates the voltmeter. (**D**) Resistance at the CNP, $V_{bg} = 0$ V, in the same contact configuration as in (C) versus magnetic field. The helical plateau is observed for both two- and four-terminal resistances between 1 T and about 6 T.

would be vanishingly small in the diffusive regime (*35*), demonstrates that current is flowing on the edges of the sample. For helical edge transport, the expected nonlocal resistance is given by $R_{NL} = R_{2t}\frac{N_V}{N_I}$, where N_I and N_V are the number of helical conductor sections between the source and drain contacts along the edge of the nonlocal voltage probes and between the nonlocal voltage probes, respectively. The measured R_{NL} shown in Fig. 3C is in near agreement with the expected value $\frac{1}{6}\frac{h}{e^2}$ ($N_I = 5$ and $N_V = 1$) indicated by the dashed line. This global set of data that is reproduced on several samples (see figs. S4 to S6) therefore provides compelling evidence for helical edge transport, substantiating the F phase as the ground state at charge neutrality of substrate-screened graphene.

To assess the robustness of the helical edge transport, we conducted systematic investigations of its temperature, *T*, and magnetic-field dependences. Figure 4C displays a color map of the two-terminal resistance of sample BNGrSTO-07 measured at charge neutrality as a function of magnetic field and temperature. The expected resistance value for the contact configuration shown in the inset schematic is $R_{2t} = \frac{2}{3}\frac{h}{e^2}$. This quantized resistance value is matched over a notably wide range of temperature and magnetic field, which is delimited by the dashed black line, confirming the metallic character of the helical edge transport. Notice that, up to 200 K, the $SrTiO_3$ dielectric constant remains high enough so that dielectric screening is virtually unaffected (*33*). To ascertain the limit of quantized helical edge transport, we measured different contact configurations at several magnetic field and temperature values near the boundary of quantized transport (see fig. S7); these values are indicated in Fig. 4C by the green and red stars for quantized and not-quantized resistance, respectively. Measurements for a different contact configuration (Fig. 4B, inset) are displayed in Fig. 4, A and B, which show the two-terminal resistance versus back-gate voltage and the resistance at the charge neutrality point versus magnetic field, respectively, for various temperatures.

These data show that quantized helical edge transport withstands very high temperatures, up to 110 K, with an onset at $B \sim 1$ T virtually constant in temperature. Such a broad temperature range is comparable to WTe_2 for which a QSH effect was observed in 100-nm short channels up to 100 K (*21*). A distinct aspect of the F phase of graphene is that the helical edge channels formed by the broken-symmetry states retain their topological protection over large distances at high temperatures, namely 1.1 μm for the helical edge sections of the sample measured in Fig. 4, A to C. Various mechanisms can account for the high-temperature breakdown of the helical edge transport quantization, such as activation of bulk charge carriers or inelastic scattering processes that

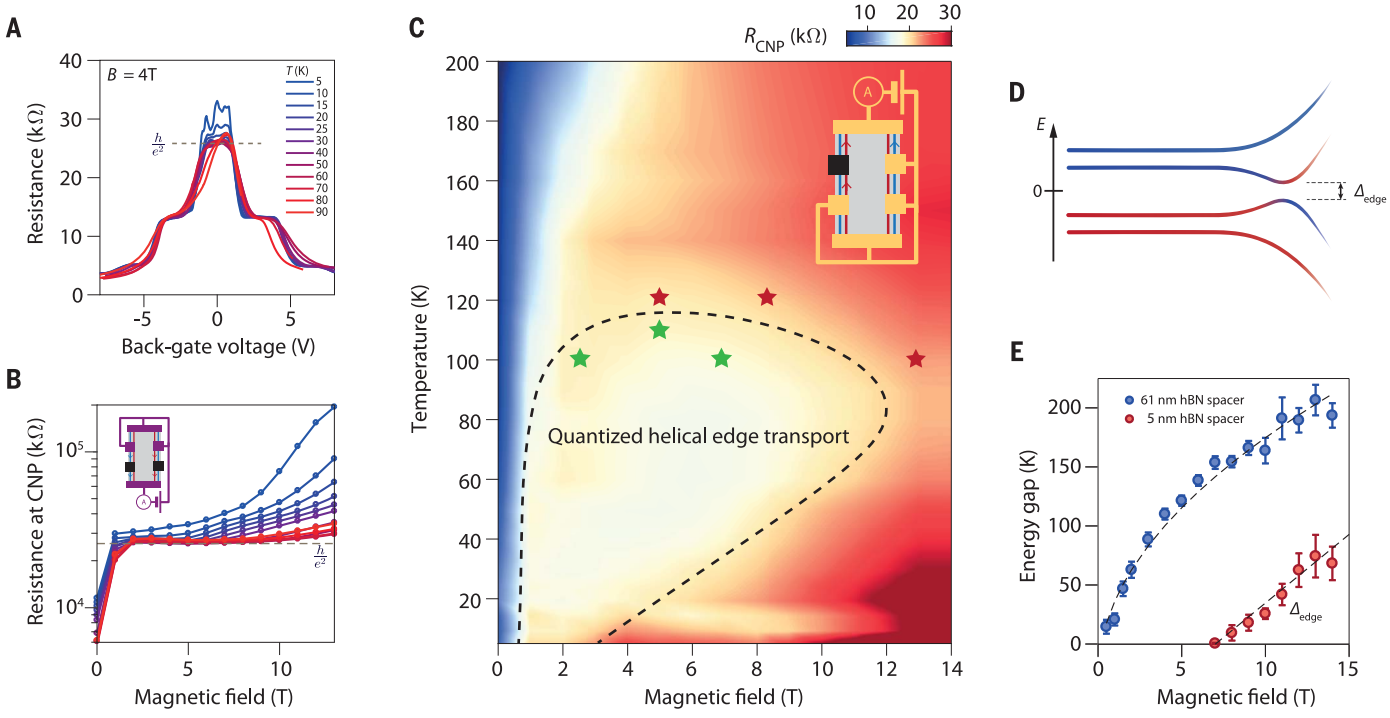

Fig. 4. Phase diagram of the helical edge transport. (**A**) Two-terminal resistance of sample BNGrSTO-07 versus back-gate voltage measured at various temperatures and a magnetic field of 4 T. The back-gate voltage is renormalized to compensate the temperature-dependence of the substrate dielectric constant (see fig. S12). (**B**) Two-terminal resistance at the CNP for the same data as in (A). The inset shows the contact configuration used in (A) and (B). (**C**) Two-terminal resistance at the CNP versus magnetic field and temperature for a different contact configuration shown in the inset. The resistance shows a plateau at the value expected for helical edge transport ($\frac{2}{3}\frac{h}{e^2}$, color coded light yellow) over a large range of temperatures and magnetic fields, that is, up to $T = 110$ K at $B = 5$ T. The stars indicate the parameters at which helical edge transport has been checked by measuring different contact configurations. (Green stars indicate quantized helical edge transport, and red stars indicate deviation to quantization at the CNP.) The dashed curve is a guide for the eye showing the approximate limits of the quantized helical edge transport of the F phase. (**D**) Schematic of the edge dispersion of the zeroth Landau level broken-symmetry states showing the opening of a gap at the edge. (**E**) Activation energy at the charge neutrality point versus magnetic field measured in samples BNGrSTOVH-02 (red dots) and BNGrSTO-09 (blue dots), which have hBN spacers of 5 and 61 nm, respectively. The dashed lines are a linear fit for BNGrSTOVH-02 and a fit of the dependence $\alpha\sqrt{B} - \Gamma$ for BNGrSTO-09. The prefactor $\alpha = 64$ KT$^{-1/2}$ corresponds to a disorder-free gap $\Delta = 0.4\mathcal{E}_C$, and the intercept $\Gamma = 27$ K describes the disorder-broadening of the Landau levels, which is consistent with the sample mobility (*33*).

break the U(1) spin-symmetry of the QHTI (*23*). Because the former mechanism would reduce resistance by opening conducting bulk channels, the upward resistance deviation upon increasing T rather points to inelastic processes that do not conserve spin-polarization. Consequently, this suggests that quantized helical edge transport may be retained at even higher temperatures for lengths below 1 μm.

Interestingly, the high magnetic field limit in Fig. 4C is temperature dependent. The lower the temperature, the lower is the magnetic field at which deviations from quantization appear: At T = 4 K, we observe an increase of resistance on increasing B from about 3 T (see Fig. 2, A and C, and Fig. 4, A to C), whereas this boundary moves to 11 T at T = 80 K. For $B \gtrsim 3$T, the resistance exhibits an activated insulating increase with lowering temperature, with a corresponding activation energy that increases linearly with B (see Fig. 4E, red dots; the data are taken on a different sample exhibiting an onset to insulation at $B \simeq 7$ T). Such a behavior indicates a gap opening in the edge excitation spectrum as illustrated in the Fig. 4D schematic, breaking down the helical edge transport at low temperatures. This linear B dependence of the activation energy further correlates with the high magnetic field limit of the helical edge transport in Fig. 4C, providing an explanation for why the boundary for quantized helical edge transport increases to higher magnetic field with increasing temperature.

The origin of the gap in the edge excitation spectrum is most likely rooted in the enhancement of correlations with magnetic field. An interaction-induced topological quantum phase transition from the QHTI to one of the possible insulating, topologically trivial quantum Hall ground states with spin- or charge-density-wave order is a possible scenario (*23*). Such a transition is expected to occur without closing the bulk gap (*8*, *23*), which we confirmed through bulk transport measurements performed in a Corbino geometry (see fig. S8). Yet, the continuous transition involves complex spin and isospin textures at the edges, thanks to the B-enhanced isospin anisotropy (*36*), yielding the edge gap detected in Hall bar geometry. Furthermore, the reentrance of the helical edge transport upon increasing temperature may point to a nontrivial temperature dependence of the bulk F phase. Another scenario relies on the helical Luttinger liquid (*37*) behavior of the edge channels, for which a delicate interplay between B-enhanced correlations, disorder, and coupling to bulk charge-neutral excitations may also yield activated insulating transport (*38*).

To firmly demonstrate the key role of the $SrTiO_3$ dielectric substrate in the establishment of the F phase, we conducted identical measurements on a sample made with a 60-nm-thick hBN spacer, much thicker than l_B at the relevant magnetic fields of this study, so that screening by the substrate is irrelevant in the quantum Hall regime. Shown in Fig. 2C with the blue dots, the resistance at the charge neutrality point for this sample diverges strongly upon applying a small magnetic field, thus clearly indicating an insulating ground state without edge transport. Systematic study of the activated insulating behavior yields an activation gap that grows as $\sqrt{B}$ (blue dots in Fig. 4E and fig. S9), as expected for a charge excitation gap that scales as the Coulomb energy $\mathcal{E}_C = e^2/4\pi\epsilon_0\epsilon_{BN}l_B$, where ϵ_0 and ϵ_{BN} are the vacuum permittivity and the relative permittivity of hBN, respectively. These control experiments indicate that the F phase emerges as a ground state owing to a substantial reduction of the electron-electron interactions by the high–dielectric constant environment.

Understanding the substrate-induced screening effect for our sample geometry requires electrostatic considerations that take into account the ultrathin hBN spacer between the graphene and the substrate (*33*). The resulting substrate-screened Coulomb energy scale $\tilde{\mathcal{E}}_C = \mathcal{E}_C \times S(B)$ is suppressed by a screening factor $S(B) = 1 - \frac{\epsilon_{STO} - \epsilon_{BN}}{\epsilon_{STO} + \epsilon_{BN}} \frac{l_B}{\sqrt{l_B^2 + 4d_{BN}^2}}$, where ϵ_{STO} is the relative permittivity of $SrTiO_3$. As a result, electrons in the graphene plane are subject to an unusual B-dependent screening that depends on the ratio l_B/d_{BN} and is most efficient at low magnetic field (fig. S11). Importantly, despite the huge dielectric constant of $SrTiO_3$ of the order of $\epsilon_{STO} \approx 10^4$ (fig. S3), $\tilde{\mathcal{E}}_C$ is scaled down by a factor 10 for $l_B/d_{BN} = 4$, owing to the hBN spacer, which is still a substantial reduction of the long-range Coulomb interaction.

How such a screening affects the short-range, lattice-scale contributions of the Coulomb and electron-phonon interactions that eventually determine the energetically favorable ground state is a challenging question. Theory states that, in first approximation, these short-range anisotropy terms should promote the spin-polarized F phase (*24*). However, more advanced calculations show that the long-range part of the Coulomb interaction can drastically modify the short-range anisotropy terms by means of renormalization effects (*39*, *40*), resulting in unpredictable changes of their amplitudes and signs (*24*). This renormalization of the anisotropy terms is taken as an argument to explain why an insulating ground state, possibly the canted-antiferromagnetic state, is experimentally observed in usual graphene samples instead of the F phase (*24*). In our experiment, the presence of the hBN spacer between the graphene and the substrate precludes the substrate to screen at the lattice scale and should thus not modify a priori the short-range interactions. Only the long-range part of the Coulomb interaction is affected by the remote substrate. Given the above, we conjecture that in our graphene samples, the substantial reduction of the long-range part of the Coulomb interaction by the substrate screening suppresses the renormalization effects, therefore restoring the F phase as the ground state at charge neutrality. Interestingly, such an indirect mechanism opens exciting perspectives: Enhancing the Coulomb energy scale $\tilde{\mathcal{E}}_C$ by decreasing the ratio l_B/d_{BN}—that is, by increasing the magnetic field or d_{BN}—can induce a topological quantum phase transition from the QHTI ferromagnetic phase to an insulating, trivial quantum Hall ground state, a type of transition hitherto little addressed theoretically (*23*).

Finally, our work demonstrates that the F phase in screened graphene, which emerges at low magnetic field, provides a prototypical, interaction-induced topological phase, exhibiting notably robust helical edge transport in a wide parameter range. The role of correlations in the edge excitations, which are tunable by means of the magnetic field and an unusual B-dependent screening, should be of fundamental interest for studies of zero-energy modes in superconductivity-proximitized architectures constructed on the basis of helical edge states (*41*–*43*). We further expect that substrate-screening engineering, tunable by means of the hBN spacer thickness, could have implications for other correlated 2D systems whose ground states and (opto)electronic properties are strongly influenced by their dielectric environment.

REFERENCES AND NOTES

1. M. Z. Hasan, C. L. Kane, *Rev. Mod. Phys.* **82**, 3045–3067 (2010).
2. X.-L. Qi, S.-C. Zhang, *Rev. Mod. Phys.* **83**, 1057–1110 (2011).
3. D. C. Tsui, H. L. Stormer, A. C. Gossard, *Phys. Rev. Lett.* **48**, 1559–1562 (1982).
4. R. Willett *et al.*, *Phys. Rev. Lett.* **59**, 1776–1779 (1987).
5. X. Du, I. Skachko, F. Duerr, A. Luican, E. Y. Andrei, *Nature* **462**, 192–195 (2009).
6. K. I. Bolotin, F. Ghahari, M. D. Shulman, H. L. Stormer, P. Kim, *Nature* **462**, 196–199 (2009).
7. P. Maher *et al.*, *Nat. Phys.* **9**, 154–158 (2013).
8. A. F. Young *et al.*, *Nature* **505**, 528–532 (2014).
9. D.-K. Ki, V. I. Fal'ko, D. A. Abanin, A. F. Morpurgo, *Nano Lett.* **14**, 2135–2139 (2014).
10. J. Falson *et al.*, *Nat. Phys.* **11**, 347–351 (2015).
11. A. Zibrov *et al.*, *Nat. Phys.* **14**, 930–935 (2018).
12. Y. Kim *et al.*, *Nat. Phys.* **15**, 154–158 (2019).
13. K. Yang, S. Das Sarma, A. H. MacDonald, *Phys. Rev. B* **74**, 075423 (2006).
14. K. Nomura, A. H. MacDonald, *Phys. Rev. Lett.* **96**, 256602 (2006).
15. A. F. Young *et al.*, *Nat. Phys.* **8**, 550–556 (2012).
16. D. A. Abanin, P. A. Lee, L. S. Levitov, *Phys. Rev. Lett.* **96**, 176803 (2006).
17. H. A. Fertig, L. Brey, *Phys. Rev. Lett.* **97**, 116805 (2006).
18. M. König *et al.*, *Science* **318**, 766–770 (2007).
19. I. Knez, R.-R. Du, G. Sullivan, *Phys. Rev. Lett.* **107**, 136603 (2011).
20. Z. Fei *et al.*, *Nat. Phys.* **13**, 677–682 (2017).

21. S. Wu *et al*., . *Science* **359**, 76–79 (2018).
22. K. Hatsuda *et al*., *Sci. Adv.* **4**, eaau6915 (2018).
23. M. Kharitonov, S. Juergens, B. Trauzettel, *Phys. Rev. B* **94**, 035146 (2016).
24. M. Kharitonov, *Phys. Rev. B* **85**, 155439 (2012).
25. J. Alicea, M. P. A. Fisher, *Phys. Rev. B* **74**, 075422 (2006).
26. I. F. Herbut, *Phys. Rev. B* **75**, 165411 (2007).
27. I. F. Herbut, *Phys. Rev. B* **76**, 085432 (2007).
28. J. Jung, A. H. MacDonald, *Phys. Rev. B* **80**, 235417 (2009).
29. J. D. Sanchez-Yamagishi *et al*., *Nat. Nanotechnol.* **12**, 118–122 (2017).
30. T. Sakudo, H. Unoki, *Phys. Rev. Lett.* **26**, 851–853 (1971).
31. N. J. G. Couto, B. Sacépé, A. F. Morpurgo, *Phys. Rev. Lett.* **107**, 225501 (2011).
32. L. Wang *et al*., *Science* **342**, 614–617 (2013).
33. See supplementary materials.
34. A. Roth *et al*., *Science* **325**, 294–297 (2009).
35. D. A. Abanin *et al*., *Science* **332**, 328–330 (2011).
36. M. Kharitonov, *Phys. Rev. B* **86**, 075450 (2012).
37. C. Wu, B. A. Bernevig, S.-C. Zhang, *Phys. Rev. Lett.* **96**, 106401 (2006).
38. P. Tikhonov, E. Shimshoni, H. A. Fertig, G. Murthy, *Phys. Rev. B* **93**, 115137 (2016).
39. I. L. Aleiner, D. E. Kharzeev, A. M. Tsvelik, *Phys. Rev. B* **76**, 195415 (2007).
40. D. M. Basko, I. L. Aleiner, *Phys. Rev. B* **77**, 041409 (2008).
41. L. Fu, C. L. Kane, *Phys. Rev. B* **79**, 161408 (2009).
42. F. Zhang, C. L. Kane, *Phys. Rev. Lett.* **113**, 036401 (2014).
43. P. San-Jose, J. L. Lado, R. Aguado, F. Guinea, J. Fernández-Rossier, *Phys. Rev. X* **5**, 041042 (2015).
44. L. Brey, H. A. Fertig, *Phys. Rev. B* **73**, 195408 (2006).
45. L. Veyrat *et al*., Data for Helical quantum Hall phase in graphene on $SrTiO_3$. Zenodo (2020); doi:10.5281/zenodo.3583364.

ACKNOWLEDGMENTS

We thank H. Courtois, M. Goerbig, M. Kharitonov, A. MacDonald, and A. Grushin for valuable discussions. Samples were prepared at the Nanofab facility of the Néel Institute. **Funding:** This work was supported by the H2020 ERC grant *QUEST* no. 637815. K.W. and T.T. acknowledge support from the Elemental Strategy Initiative conducted by the MEXT, Japan; A3 Foresight by JSPS; and the CREST (JPMJCR15F3), JST. Z.H. acknowledges support from the National Key R&D Program of China (2019YFA0307800 and 2017YFA0206302); the National Natural Science Foundation of China (NSFC) with grants 11504385, U1932151, and 51627801; and the Program of State Key Laboratory of Quantum Optics and Quantum Optics Devices (no. KF201816). **Author contributions:** L.V. and X.L. made the hBN/graphene/hBN heterostructures. L.V., C.D., and A.C. made the sample fabrication. L.V., C.D., Z.H., and B.A.P. performed the experiments. F.G. provided technical support on the experiments. K.W. and T.T. grew the hBN crystals. L.V., B.A.P., H.S., and B.S. analyzed the data. B.S. conceived the study, supervised the project, and wrote the paper with the input of all co-authors. **Competing interests:** The authors declare that they have no competing financial interests. **Data and materials availability:** All data described here are available at Zenodo (*45*).

SUPPLEMENTARY MATERIALS

science.sciencemag.org/content/367/6479/781/suppl/DC1
Materials and Methods
Supplementary text
Figs. S1 to S12
Table S1
References (*46*–*49*)

30 April 2019; accepted 14 January 2020
10.1126/science.aax8201

Science

Helical quantum Hall phase in graphene on $SrTiO_3$

Louis Veyrat, Corentin Déprez, Alexis Coissard, Xiaoxi Li, Frédéric Gay, Kenji Watanabe, Takashi Taniguchi, Zheng Han, Benjamin A. Piot, Hermann Sellier and Benjamin Sacépé

Science **367** (6479), 781-786.
DOI: 10.1126/science.aax8201

Controlling the interactions

Near charge neutrality and subject to perpendicular magnetic fields, graphene is expected to become a ferromagnet with edge states not unlike those in two-dimensional topological insulators. Observing this effect experimentally has proven tricky because very large magnetic fields are needed to overcome the effect of electron-electron interactions, which drive the system to competing states. Instead of amping up the field, Veyrat *et al.* placed their graphene samples on a substrate made out of strontium titanate, which effectively screened the interactions. Transport measurements confirmed the formation of the characteristic edge states.

Science, this issue p. 781